Science Advances
AAAS

advances.sciencemag.org/cgi/content/full/5/7/eaaw0409/DC1

Supplementary Materials for

Antisymmetric magnetoresistance in van der Waals Fe_3GeTe_2/graphite/Fe_3GeTe_2 trilayer heterostructures

Sultan Albarakati, Cheng Tan, Zhong-Jia Chen, James G. Partridge, Guolin Zheng, Lawrence Farrar, Edwin L. H. Mayes, Matthew R. Field, Changgu Lee, Yihao Wang, Yiming Xiong, Mingliang Tian, Feixiang Xiang, Alex R. Hamilton, Oleg A. Tretiakov, Dimitrie Culcer*, Yu-Jun Zhao*, Lan Wang*

*Corresponding authors. Email: lan.wang@rmit.edu.au (L.W.); zhaoyj@scut.edu.cn (Y.-J.Z.); d.culcer@unsw.edu.au (D.C.)

Published 5 July 2019, *Sci. Adv.* **5**, eaaw0409 (2019)
DOI: 10.1126/sciadv.aaw0409

This PDF file includes:

Section S1. Ohmic contacts

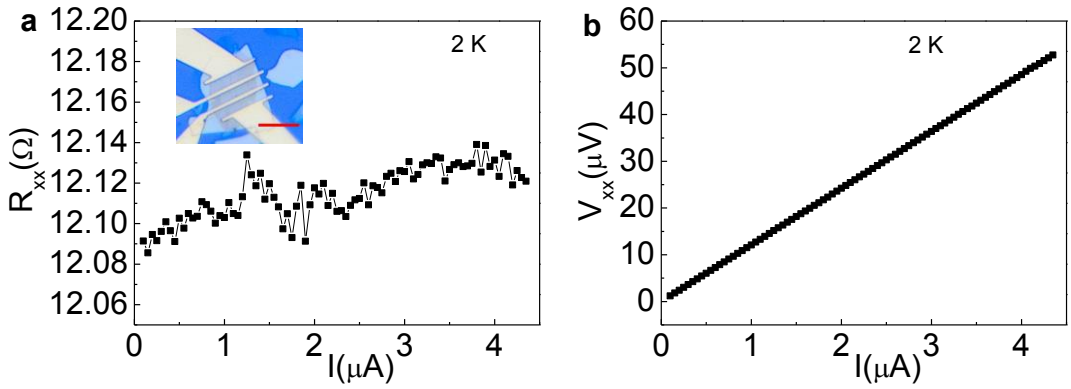

Fig. S1. Ohmic contact confirmation. (a) R_{xx} vs current curve at 2 K. Inset is an image of the device under test with a scale bar representing 10 μm. **(b)** The corresponding I-V curve derived from **(a).**

Section S2. Dimensions of all FGT/graphite/FGT devices

Table S1. Dimensions of all FGT/graphite/FGT devices.

Device label	Upper FGT(nm)	Lower FGT(nm)	Graphite (nm)	Length × Width (μm×μm)
FPC1	21.7	42	7.6	8×5.5
FPC2	16	73.5	8.7	8.1×6.2
FPC3	16.2	108	3.5	9.4×4.1
FPC4	22	142	11	11.9×11.5
FPC5	48.9	114	9.2	7.0×1.5
FPC6	16.4	78.5	5.4	8.3× 4.8
FPC7	14.5	95.6	5.7	7.8×2.1
FPC8	21.2	94.2	4.6	6.8×5.5
FPC9	45	93.5	7	7.5×4.5
FPC10	27.2	89	2.9	6.5×3.7
FPC11	18.7	64	8.4	10.5×5.2

Section S3. Transmission electron microscopy (TEM) on the heterostructures

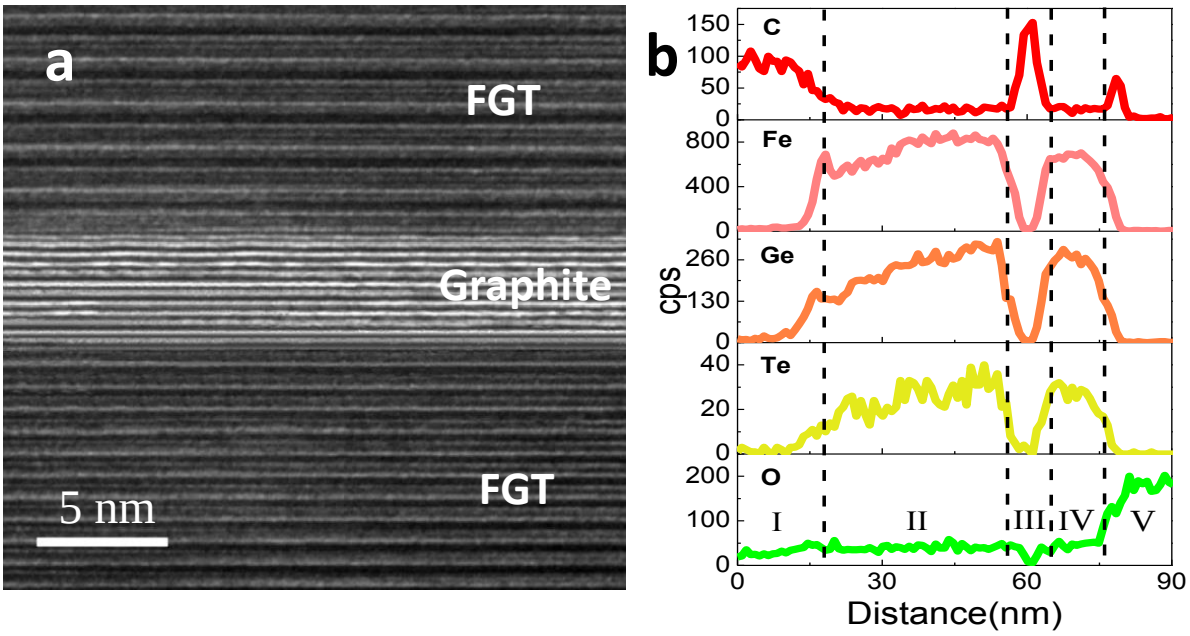

Fig. S2. TEM on FGT/graphite/FGT heterostructure. (a) The cross-sectional TEM image obtained from a FGT/Graphite/FGT heterostructure. The TEM sample was prepared by FIB based ion milling. Interfaces between the graphite layer and the FGT layers are clearly observed. **(b)** EDX line-scan of the cross-sectional TEM image. Section I is the top protective layer composed of carbon. Sections II & IV are the FGT layers. Section III is the graphite layer. Section V is the SiO_x (substrate) layer. The oxygen content is lower in the graphite layer and higher in FGT layers because the TEM sample was necessarily exposed to ambient and the graphite layer oxidizes less readily than the FGT.

Section S4. The effect of graphite layer etch and samples with weak interlayer coupling

Etching the graphite is very important. As the resistivity values of the FGT and graphite are ~10^{-8} Ω·cm^{-1} and ~10^{-4} Ω·cm^{-1}, respectively, current flow will occur mostly through the graphite layer if the horizontal size of the graphite layer is larger than the FGT layers.

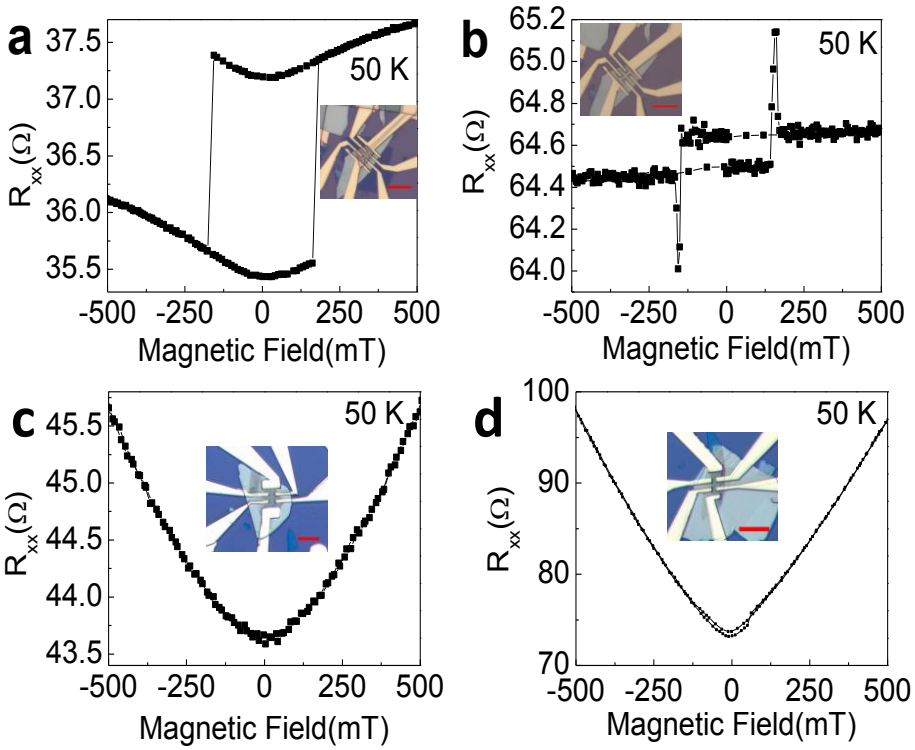

Fig. S3. The effect of graphite layer etch and samples with weak interlayer coupling. (a) R_{xx}(B) curve for sample FPC6 before the graphite layer was etched. The magnetoresistance of the graphite is very large, indicating that most of the electrons pass through the graphite layer directly. In this condition, the antisymmetric MR effect cannot be observed. Inset shows the device covered with a PMMA masking layer prior to O_2 etching. The scale bar represents 10 μm. **(b)** R_{xx}(B) curve from sample FPC6 after the graphite layer was etched. An Ar plasma was used to etch the graphite layer after the metal deposition. Before the etch, a PMMA etching mask is fabricated by e-beam lithography. The electrons mainly pass through the tri-layer region and thus the antisymmetric MR effect can be displayed. Inset scale bar represents 10 μm. (**c and d**) Field dependent R_{xx} of another 2 samples with etched graphite layer but contaminated interfaces between the graphite layers and the FGT layers. These samples only exhibit magnetoresistance from graphite. The inset red scale bars represent 10 μm. As shown in our experiments, a clean FGT/graphite interface is essential for the antisymmetric MR effect, which is indicative of the importance of the magnetic proximity effect. A short-ranged magnetic coupling at the FGT/graphite interface and/or induced magnetic order in the graphite layer may also affect the antisymmetric MR effect in addition to the spin-polarized 2DEG at the interface.

Section S5. Fabrication of a symmetric Hall bar device based on FIB milling

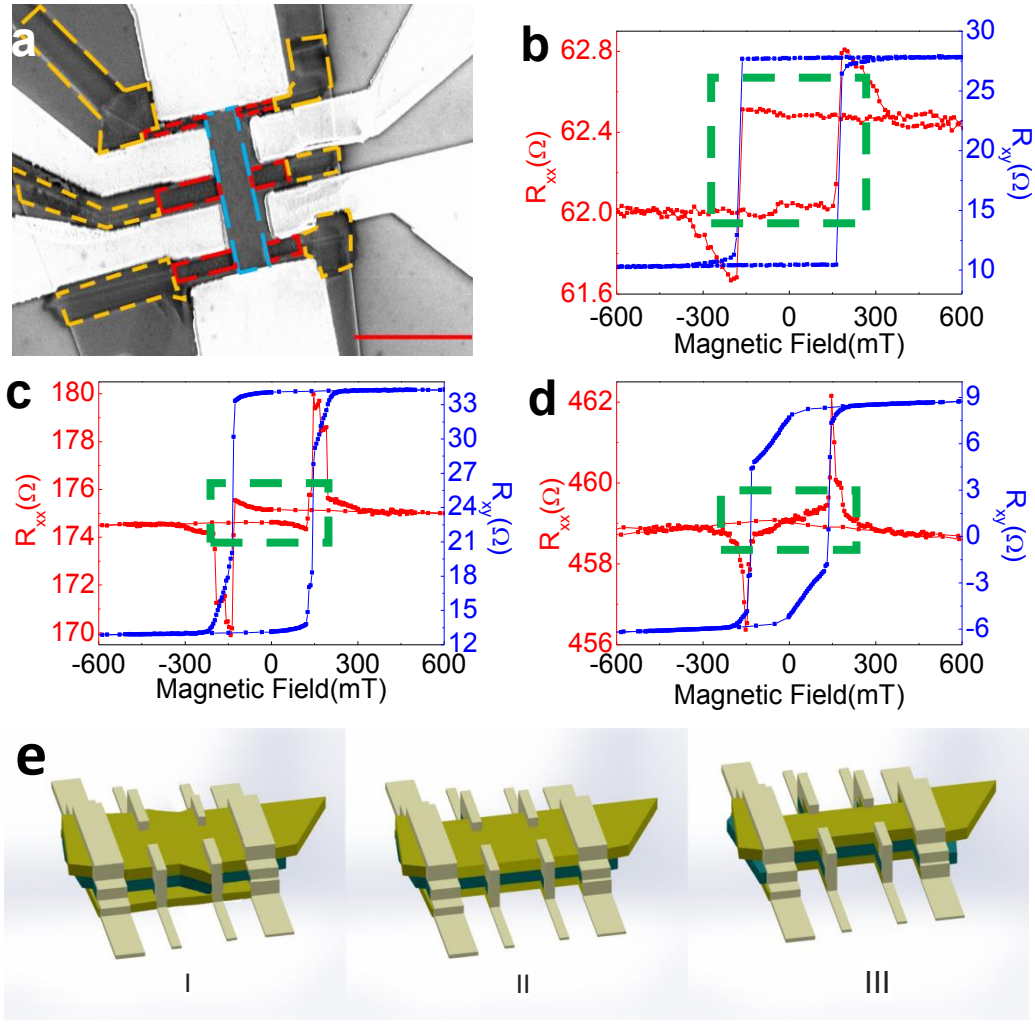

Fig. S4. R_{xx} and R_{xy} of an FIB-etched FGT/graphite/FGT device at 50 K. (**a**) Scanning electron microscope image of the FIB-etched device. The orange, red and blue dashed lines identify the etched region in the first etching step, the etched region in the second etching step, and the final un-etched region, respectively. The un-etched region remained non-exposed to the FIB. The scale bar represents 5 μm. (**b**) Field dependent R_{xx} and R_{xy} curves for the sample before the FIB etch process. At this step, only the graphite layer was etched by O_2 plasma (The blue layer in the Fig. S4e). (**c**) Field dependent R_{xx} and R_{xy} curves from the sample after the first etch. At this step, the heterostructure was etched into a symmetric shape, but not a strict Hall bar structure. (**d**) Field dependent R_{xx} and R_{xy} curves measured from the sample after the second etch. The device exhibited a standard Hall bar structure at this stage. From figure **b** to **d**, the "loops" in the green dashed line box gradually close, indicating a 3-state MR effect. (**e**) Schematic diagrams of each etch step. I, II, III representing **b**, **c**, **d,** respectively.

Section S6. Transport measurement for other samples

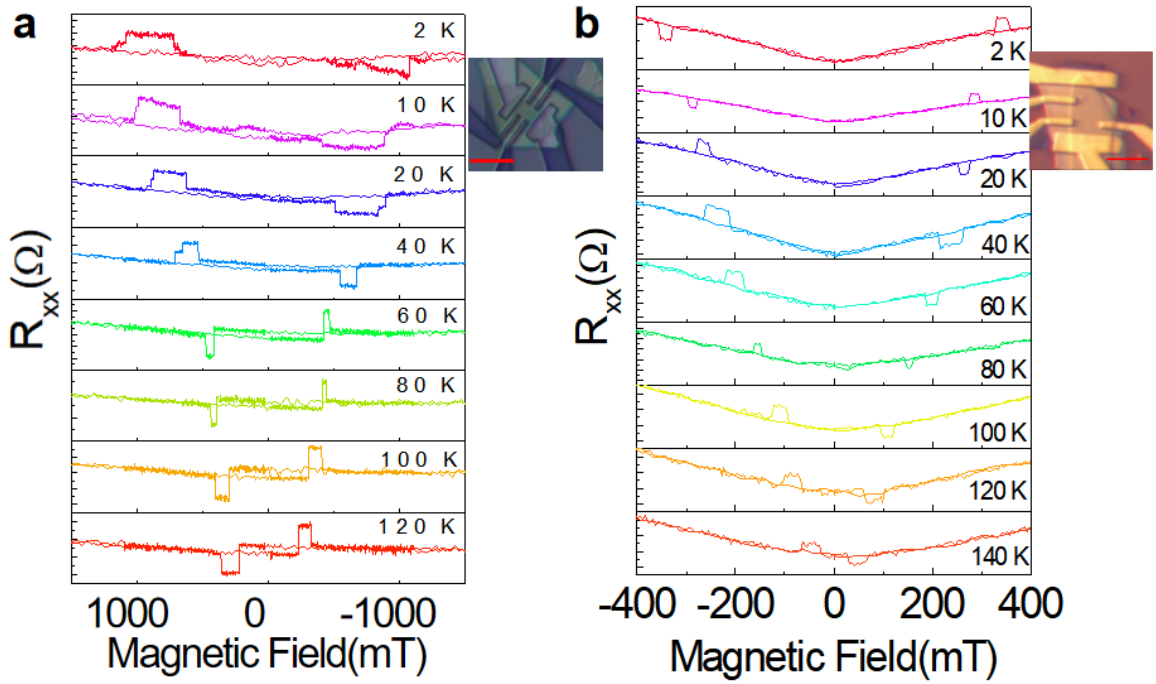

Fig. S5. Measurements for FPC1 and FPC9. (a) $R_{xx}(B)$ curves at various temperatures measured from sample FPC1 tilted at 85°. This data was obtained from the same sample providing the data in figure 2 and figure 3 in the main text. The high resistance state and low resistance state switched when the temperature decreased from 60 K to 40 K due to the coercive field evolution of the top and bottom FGT layers. Some plateaus in the data obtained below 60 K also show multi-step behaviour. **(b)** $R_{xx}(B)$ curves from the sample FPC9 shown in the inset at different temperatures and with the magnetic field perpendicular to the sample surface. The high resistance state and low resistance state also switch between 20 K and 10 K. The magnitudes of the peaks remain similar at different temperatures. The scale bars represent 10 μm. Top FGT thickness: 45 nm, bottom FGT thickness: 93.5 nm, graphite thickness: 7 nm.

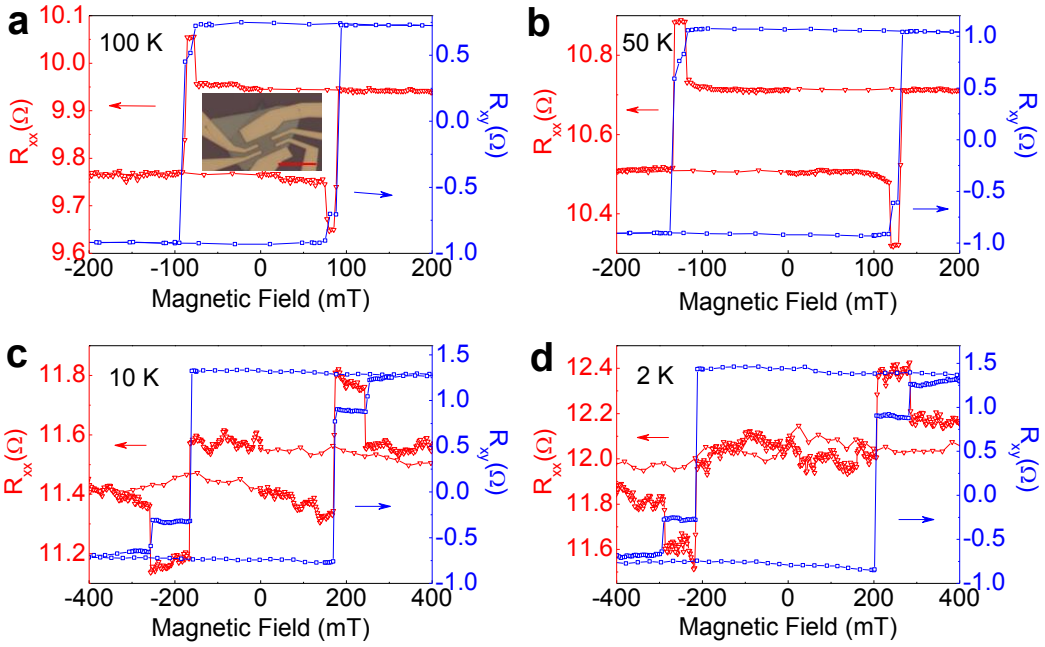

Fig. S6. Measurement for an asymmetric sample FPC2 (the anomalous Hall signal is large). (a)(b) $R_{xx}(B)$ and $R_{xy}(B)$ curves measured from the sample at 100 K and 50 K. The contribution from the anomalous Hall effect is large in the R_{xx} measurements. Inset of **(a)** shows an optical image of the device, the scale bar represents 10 μm. Top FGT thickness: 16.2 nm, bottom FGT thickness: 73.5 nm, graphite thickness: 8.7 nm. **(c)(d)** $R_{xx}(B)$ and $R_{xy}(B)$ curves measured from the sample at 10 K and 2 K. The direction of the plateaus in R_{xx} switched in comparison with that observed at 50 K and 100 K, indicating different temperature dependence of the coercivity in the two FGT layers.

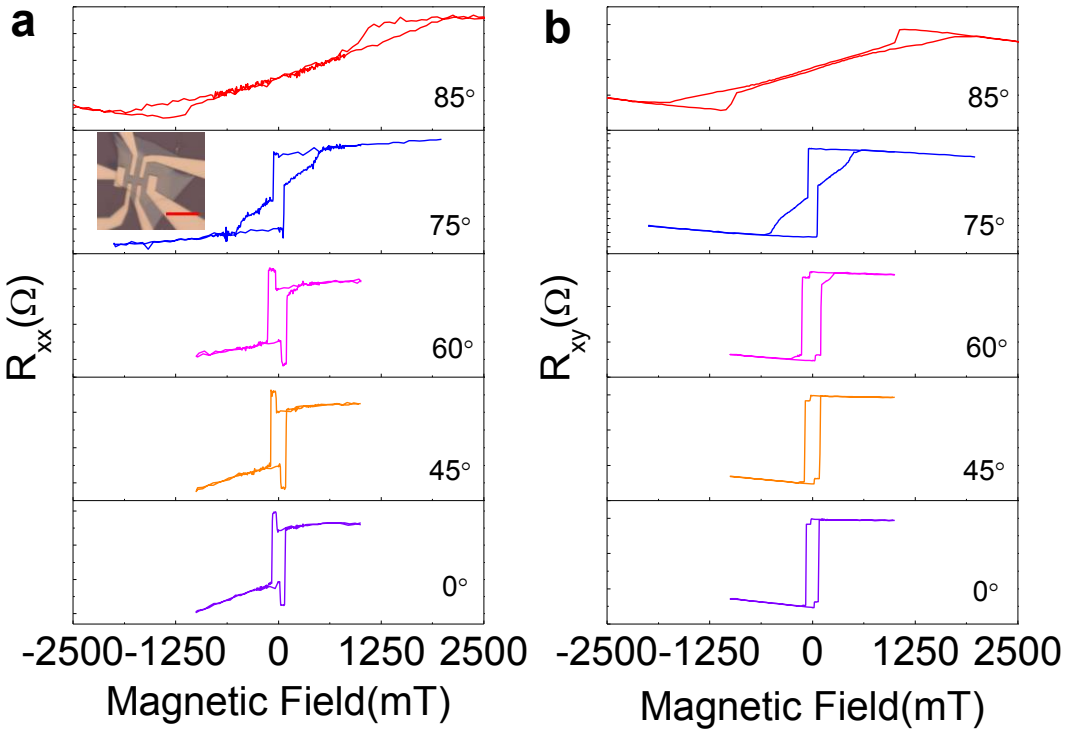

Fig. S7. Angle-dependent curves at 50 K for sample FPC11, with top and bottom FGT touching each other. (a) $R_{xx}(B)$ curves for the sample at various angles. When the angle > 60º, the plateaus nearly fade away and the shapes of $R_{xx}(B)$ curves are nearly the same as the corresponding $R_{xy}(B)$ curves. This is because the domain of the top and bottom FGT layer are coupled together and flip at the same time when the angle > 60º. **(b)** Corresponding $R_{xy}(B)$ curves. Inset of **(a)** shows an optical image of the device with scale bar representing 10 μm. Top FGT thickness: 18.7 nm, bottom FGT thickness: 64 nm, graphite thickness: 8.4 nm.

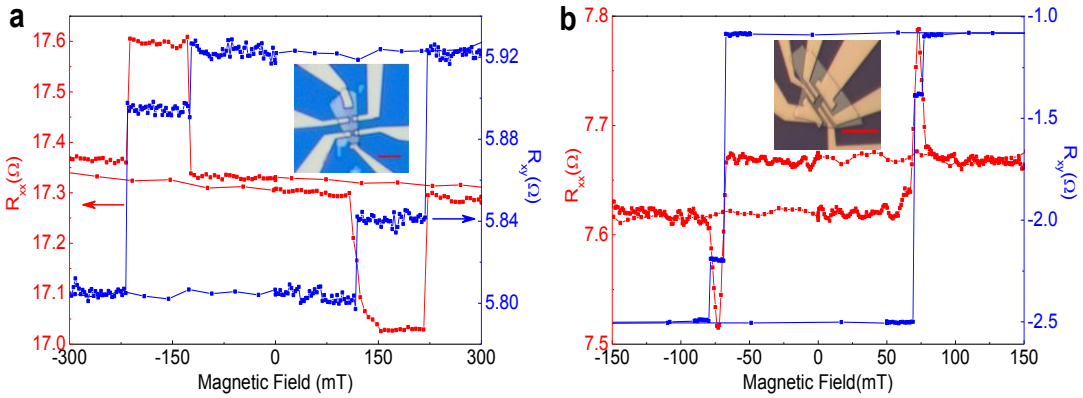

Fig. S8. R_{xx}(B) and R_{xy}(B) curves for two samples with relatively larger $\Delta R_{xx}/R_{xx}$ value at 50 K. (a) Sample FPC7, $\Delta R_{xx}/R_{xx}$ value is ~1.5%. Inset is the optical image for the device, the scale bar represents 5 μm. Top FGT thickness: 14.5 nm, bottom FGT thickness: 95.6 nm, graphite thickness: 5.7 nm. **(b)** Sample FPC8 exhibiting $\Delta R_{xx}/R_{xx}$ value of ~1.4%. The scale bar in the inset optical image represents 10 μm. Top layer thickness: 21.2 nm, bottom layer thickness: 94.2 nm, graphite thickness: 4.6 nm

Section S7. Tentative resistor model

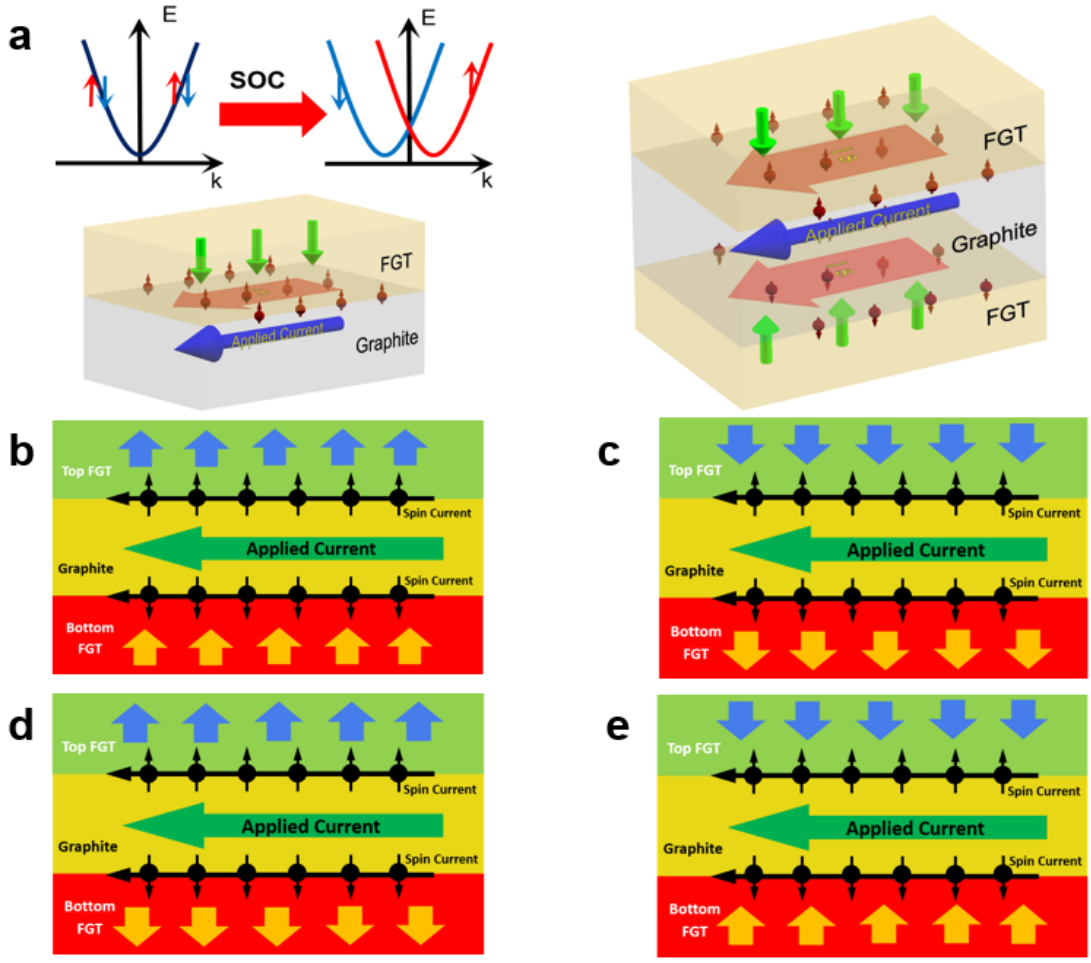

Fig. S9. Tentative resistor model. (a) Schematic diagram of the Rashba spin splitting induced spin distribution in the heterostructure. The green arrows represent the direction of magnetisation in the FGT. (**b and c**) The parallel magnetisation in a FGT/graphite/FGT heterostructure. The devices show intermediate interfacial conductance. (**d and e**) The antiparallel magnetisation in a FGT/graphite/FGT heterostructure. The devices show low and high interfacial conductance, respectively.

Section S8. Band structure calculation

8.1 Computational methods

In this work, the Vienna Ab-initio Simulation Package (VASP) software package was used for first-principles calculations based on density functional theory (DFT) with the projector augmented wave method. The Predew-Burke-Ernzerhof (PBE) type generalized gradient approximation (GGA) was chosen to describe the exchange-correlation functional. For the electronic properties of bulk Fe_3GeTe_2, an energy cutoff of 310 eV was used for the plane wavefunction basis and the Brillouin Zone was sampled using a $7 \times 7 \times 2$ k-point mesh following the Monkhorst-Pack scheme. The surface states and surface spin texture were calculated using the WannierTools package and the tight-binding model Hamiltonian was derived from the Wannier functions.

8.2 Results and discussion

Bulk Fe_3GeTe_2 hosts a layered structure stacked along the [001] direction and the (001) surface can be regarded as a hexagonal lattice similar to graphene. We calculated the band structures with and without the SOC effect for the ferromagnetic Fe_3GeTe_2.

In the absence of SOC, the bands are decoupled into two spin channels. The Fermi level is buried deep in the bands in both spin channels, reflecting their metallic characteristics. After introducing the SOC effect, the bands split and a small gap opens. The projected band structures on the (001) surface are shown in fig. S10(a), which is plotted along the k-path depicted in fig. S10(b).

To study the surface spin behaviors of Fe_3GeTe_2 under the influence of intrinsic magnetic moment, we also calculated the surface Fermi arc and surface spin texture of Fe_3GeTe_2 with SOC. As illustrated in fig. S10(b), distinct metallic features of both bulk and surface bands lead to the complex images of Fermi surface and surface Fermi arc, while the magnetization is mostly relaxed in the [001] direction.

By calculating the spin texture of surface states near the high symmetry points of Γ and K in the two-dimension Brillouin zone, we found that the spin is highly polarized along the z axis. The spin polarization directions can go up or down along the z axis for each band in the surface. For example, clear surface states with downward direction of spin polarization near Γ point are observed, as shown in fig. S10(c). Near K point (-K), the Fermi arcs form two loops centered on K (-K) point and exhibit similar spin polarization with Γ point, as shown in fig. S10(d). Except for

the clear surface states near the k-points Γ and K, some surface states within the bulk bands are found to exhibit upward spin polarization direction. We also found that, the spin direction will be reversed if the magnetization direction is reversed.

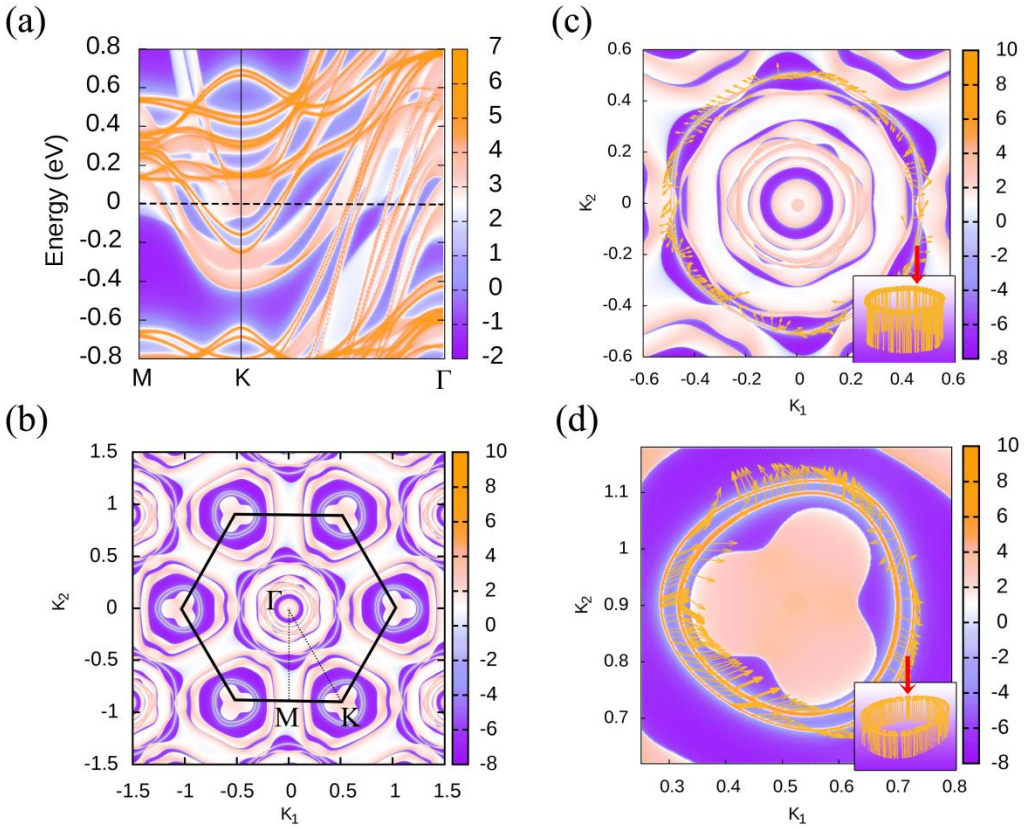

Fig. S10. Surface states and surface spin texture of FGT. (a) Surface states projected on the (001) surface along the k-path M-K-Γ as depicted in **(b)**. **(b)** Fermi arcs projected on the (001) surface and the first Brillouin zone of the slab systems. **(c)** Fermi arcs and surface spin texture around the Γ. **(d)** Fermi arcs and surface spin texture around the K point. The spin texture of the surface states in three dimension momentum space are shown in the insets.

Section S9. Discussion about the angle-dependent results in Fig. 3

To obtain the antisymmetric MR effect in the FGT/graphite/FGT heterostructures, top and bottom FGT layers with different coercivities are required. As the coercivities of the FGT nanoflakes are related to their thicknesses, the antisymmetric MR is readily observed in heterostructures composed of FGT nanoflakes with different thicknesses.

We used a pick-up technique to fabricate the devices. In this technique, we first use the top FGT layer to pick up the graphite layer and then use the top FGT/graphite structure to pick up the bottom FGT layer. Finally, we release the heterostructures onto the Si/SiO_x substrate. We prefer to choose thin FGT flakes as the top layer because a thin FGT nanoflake is transparent. In the stacking process, we can see through the top thin FGT layer and align the graphite layer (also thin and transparent) and the bottom FGT layer more easily.

It is well known that the coercivity of a ferromagnet is strongly related to the microstructure of the magnet. For a single crystalline FGT nanoflake, as shown in our previous work [*Nat. Commun.* 9, 1554 (2018)], the coercivity is mainly determined by the perpendicular anisotropy. However, the Fe stoichiometry, the thickness of the flake, the defects in the flake, the shape of the flake and the surface oxidation on the top FGT layer all contribute to a change in the coercivity.

When θ (the angle between the magnetic field and the perpendicular direction to the device surface) is small, the magnetic moments in an FGT nanoflake rotate coherently and show a single domain behavior (except in the regime near the coercivity), therefore the coercivity is mainly determined by the perpendicular anisotropic energy (K_A). If the K_A value of the thinner FGT layer is smaller than that of the thicker FGT layer, the thinner layer will have a smaller coercivity and flip first at a lower field. When the θ value increases, the magnetic moments in the FGT will tilt towards the direction parallel to the surface and the defects near the surface will pin the rotation of the magnetic moments. This effect is larger in thinner FGT flakes, because it is a surface effect, and therefore can generate the gradual evolution of the coercivity as shown in Fig. 3 in the main text. When θ is large, the rotation of magnetic moments becomes non-collinear, which also generates different coercivity changes according to the microstructure (shape, defects, surface oxidation etc.) of the flake.

In all, the evolution of the coercivity with tilt angle is determined by the complex microstructure of the FGT nanoflakes. The device in Fig. 3 shows the MR flips at $\theta = 70^{o}$ but the same effect may not appear in another device until the tilt angle is 90^{o}. Nevertheless, all these magnetic moment configurations can be confirmed from the anomalous Hall measurements. No matter how the relative coercivity of the top FGT and bottom FGT changes, the “IN” and “OUT” magnetic moment configuration determines “high” or “low” MR states.